MACHINE LEARNING
Science and Technology

PURPOSE-LED PUBLISHING™ Part of the MACHINE LEARNING Series

PAPER • OPEN ACCESS

Deep learning-driven glioblastoma diagnosis from histopathological images via single-cell segmentation and morphological analysis

To cite this article: Gonzalo Rosa-Olmeda *et al* 2025 *Mach. Learn.: Sci. Technol.* **6** 045052

View the article online for updates and enhancements.

You may also like

- Towards instance-wise calibration: local amortized diagnostics and reshaping of conditional densities (LADaR)
Biprateep Dey, David Zhao, Brett H Andrews et al.
- An atomic cluster expansion potential for twisted multilayer graphene
Yangshuai Wang, Drake Clark, Sambit Das et al.
- Detecting model misspecification in cosmology with scale-dependent normalizing flows
Aizhan Akhmetzhanova, Carolina Cuesta-Lazaro and Siddharth Mishra-Sharma

This content was downloaded from IP address 138.100.58.221 on 05/02/2026 at 11:11

MACHINE LEARNING
Science and Technology

Check for updates

OPEN ACCESS

RECEIVED
24 April 2025

REVISED
14 September 2025

ACCEPTED FOR PUBLICATION
13 November 2025

PUBLISHED
25 November 2025

Original Content from this work may be used under the terms of the Creative Commons Attribution 4.0 licence.

Any further distribution of this work must maintain attribution to the author(s) and the title of the work, journal citation and DOI.

PAPER

Deep learning-driven glioblastoma diagnosis from histopathological images via single-cell segmentation and morphological analysis

Gonzalo Rosa-Olmeda[1,5], Sara Hiller-Vallina[2,3,5], Manuel Villa[1], Massimo Salvi[4], Ricardo Gargini[2,3] and Miguel Chavarrías[1,*]

[1] Research Center on Software Technologies and Multimedia Systems, Universidad Politécnica de Madrid, 28031 Madrid, Spain
[2] Pathology and Neurooncology Unit, Hospital Universitario 12 de Octubre, 28041 Madrid, Spain
[3] Instituto de Investigación Biomédica i+12, Hospital Universitario 12 de Octubre, 28041 Madrid, Spain
[4] Biolab, PoliToBIOMed Lab, Department of Electronics and Telecommunications, Politecnico di Torino, 10129 Turin, Italy
[5] These authors contributed equally to this work.
[*] Author to whom any correspondence should be addressed.

E-mail: miguel.chavarrias@upm.es

Keywords: glioblastoma, pathological diagnosis, hematoxylin and eosin, single-cell analysis, deep learning, cell morphology

Supplementary material for this article is available online

Abstract

Glioblastoma (GBM) exhibits a high recurrence rate of 95% due to its highly infiltrative nature and marked heterogeneity, making its diagnosis challenging. These characteristics complicate the standardization of diagnostic criteria and contribute to significant interpathologist variability. In response, artificial intelligence-based tools are increasingly being developed to support the diagnostic process. This study presents a complete processing pipeline that integrates deep learning and machine learning techniques to facilitate the screening of hematoxylin and eosin-stained histopathological images, aiming to reduce the workload in pathology departments. The proposed workflow includes a convolutional neural network capable of detecting and segmenting individual cells, achieving 89.5% pixel-wise precision and a DICE coefficient (DSC) of 88.4%, indicating a high degree of spatial overlap between the predicted and reference regions. Following segmentation, a set of morphological features is extracted, including cell area, circularity, cell count, and the average distance between neighboring cells. The extracted features were subsequently used for tissue classification into tumorous and non-tumorous categories via a random forest algorithm, resulting in a high classification accuracy of 94.15%, thereby suggesting the robustness and reliability of the proposed approach. The applied methodology was validated on a cohort of 82 patients, comprising both tumor and healthy tissue, with a total of 1557 images and more than 4 million annotated cells.

1. Introduction

Gliomas are the most common primary brain tumors, accounting for around 80% of all malignant brain tumors [1]. Due to their heterogeneous nature, a thorough understanding of their histology is essential for accurate classification and prognosis [2]. In fact, the 2021 World Health Organization classification (WHO CNS 2021) stratifies gliomas from grade 1 to 4, taking into account key histological markers such as cellular atypia, mitotic activity, vascular proliferation, and necrosis [3]. In this context, morphological analysis plays a fundamental role in the identification and classification of these tumors, providing an initial assessment of their aggressiveness. Moreover, the last classification established in 2021, integrates molecular alterations, particularly mutations in the isocitrate dehydrogenase 1/2 (IDH1/2) genes. Based on these parameters, gliomas are classified into different subtypes: IDH1/2 mutant (IDHmut) oligodendroglioma (grades 2 and 3), IDHmut astrocytoma (grades 2–4) and grade

© 2025 The Author(s). Published by IOP Publishing Ltd

4 IDH1/2 wild-type (IDHwt) astrocytoma, known as glioblastoma (GBM) [3]. GBMs are the most aggressive and common glioma tumors, representing almost 50% of adult central nervous system (CNS) malignancies [4]. Despite significant advances in GBM research, the patients' prognosis remains extremely poor. The median survival for patients with GBM is only 15 months post-diagnosis, with a mere 5% surviving beyond five years [5]. Even with the current standard of care known as the STUPP protocol, which includes surgical resection followed by radiotherapy and temozolomide [6], tumor recurrence rates remain alarmingly high, exceeding 95%. This underscores the urgent need to develop accurate and accessible diagnostic tools to support pathologists in their assessment. Currently, the most widely used technique for diagnosis is H&E staining, a well-established method in histopathology [7]. This technique enables detailed visualization of nuclear morphology, potential alterations in cell division, as well as cytoplasmic components and extracellular matrix, allowing more precise tissue differentiation [8].

Extensive research has shown that tumor cells undergo significant morphological changes, such as irregularly shaped and enlarged nuclei, prominent nucleoli and reduced cytoplasmic volume, which can stain from intensely basophilic to pale range, depending on cellular metabolic activity [9, 10]. These alterations are closely associated with dynamic remodeling of cellular components that are responsible for mechanical support, such as the cytoskeleton, along with the deregulation of cellular signaling pathways [11]. The cytoskeleton, a network of filaments, provides structural integrity to cells and plays a key role in the preservation of cell shape and function [12]. Modifications in the cytoskeletal architecture directly affect cell stiffness and adhesion to the extracellular matrix, facilitating the invasive and metastatic potential of tumor cells [13]. These alterations often arise from genetic and epigenetic mutations that impact critical processes such as cell cycle progression, migration, and apoptosis [13]. Additionally, the tumor microenvironment promotes the activation of transcription factors that regulate cell adhesion and migration, driving actin cytoskeleton remodeling [14]. Actin dynamics plays a crucial role in the epithelial–mesenchymal transition, a process that improves tumor cell migration and invasion, thus contributing to cancer progression [15]. Precisely for this reason, morphological analysis of cells remains a key parameter to understand both tumor behavior and diagnosis. Notably, specific morphological features have been shown a significant correlation with patient survival [16, 17].

Glioma diagnosis and classification heavily depends on histopathology assessment using H&E staining [2, 18], a gold-standard technique that, despite its importance, is subjective and dependent on the expertise of the pathologist. Furthermore, the huge heterogeneity presented by GBM, combined with the increasing workload and time constraints in pathology services, presents a major challenge for accurate and efficient tissue classification. In recent years, to reduce this interobserver variability in diagnosis, the application of systems based on artificial intelligence (AI) has enabled more precise and reproducible diagnostic systems [19, 20]. However, AI has been used mainly for multimodal data integration [21, 22], such as genetic profiling, rather than relying exclusively on morphological characteristics. Several studies have demonstrated the potential of deep learning (DL) models for histopathological image analysis. Unger *et al* [23] concluded that extending histopathological image analysis with DL techniques and multimodal data significantly enhances diagnostic accuracy. Indeed, image segmentation plays a crucial role in this process, enabling the localization and extraction of areas containing the most relevant information for image analysis, such as malignant cells, tumor borders, and other critical tissue components, which are accurately identified and isolated for precise analysis and feature extraction. In recent years, several reviews have addressed whole slide image (WSI) analysis as the most promising method of image analysis in histopathology [24]. For instance, Jiang *et al* [25] proposed end-to-end DL models based on WSI and ResNet-18 architecture to predict prognosis (achieving a C-index of 0.715) and IDH 1/2 mutation status (with an AUC of 0.667) in adult grade 2 gliomas, addressing the challenge of limited sample size by clustering repeated random split predictions but by applying a classification of those samples instead of a cell segmentation. Complementarily, Roetzer-Pejrimovsky *et al* [21] used a modified Xception convolutional neural network in IDHwt cases, successfully demonstrating its ability to establish accurate correlations between WSI features(specifically H&E slides) and genotype–phenotype properties, including spatial mapping of transcriptional subtypes. Moreover, in works recently published such as [26], authors have relied on CNN feature extraction within an encoder from another family of neural networks called transformers to improve tissue classification performance. Peng *et al* [27] conducted an extensive review of various techniques for cellular segmentation, highlighting the strengths and limitations of each method. Nevertheless, in the broader context of neural networks, a recently published model called ConvNext [28] has demonstrated significant advancements in the CNN due to the modification in the internal architecture and the application of modern normalization and regularization methods. Overall, these advancements reveals the growing potential of DL-driven methodologies in enhancing diagnostic precision and efficiency in histopathological image analysis.

Nonetheless, despite all the advancements mentioned so far, and to the best of authors' knowledge, no comprehensive study has currently explored the use of such large-scale morphologic analysis in high grade astrocytomas. At least no study that provides detailed numerical data exclusively from morphological analysis to support the development of new tools for future research have been published. Based on that, the purpose of this research paper is to present a novel DL-based aid tool capable of distinguishing healthy and tumor tissues based on cell morphological features. Indeed, the novelty of this tool relies precisely on the ability to characterize tissue pathology based on: the distances between neighbors cells, cellular count, the circularity of each cell and its area. These features are calculated from the segmentation masks generated from the soft-max probability maps generated in the last layer of the ConvNeXt neural network. The main contributions presented in the document are therefore as follows:

- A diagnostic assistant tool based on the random forest (RF) algorithm capable of distinguishing between tumor images and healthy images with 94.56% precision metric by analyzing the morphological features extracted from histopathological images. This tool has been trained with the morphological features of 74 patients. This tool could allow a first screening of the images to reduce the workload of the pathologist.
- The proposal to incorporate the morphological feature of the distance between neighboring cells as a new analysis parameter for the diagnosis of high grade astrocytoma, which demonstrated a decision-making impact greater than 50%.
- A custom-trained DL-based semantic cell segmenter based on ConvNeXt-XL [28] that segments cell nuclei from the background on histopathological images with a precision of 89.55% and a DICE of 88.4% per pixel, trained 811 640×640 pixels patches from 15 different patients labeled by experts pathologists.
- The analysis of a proprietary database of 2651 histological images. For this study, only images marked as tumor and healthy tissue were used, resulting in a final dataset of 1557 images containing more than 4 million cells, captured from 82 meticulously selected patients, along with their clinical and molecular data. The database is composed of 62 patients with high grade astrocytoma and 20 patients with healthy tissue as control. As a novelty, the images have been captured at $10\times$ magnification to promote a contextual analysis of the tissue architecture and microenvironment.

2. Materials and methods

2.1. Patients cohort

This study includes two retrospective cohorts of patients ($n = 82$) from Hospital Universitario 12 de Octubre, Madrid table 1, Spain, diagnosed between 2012 and 2024. Tissue samples were fixed in formalin paraffin-embedded blocks and diagnosed after a thorough histological and molecular analysis. The first cohort, referred to as tumor cohort, is composed of 62 patients diagnosed with grade 4 astrocytoma, of whom 18 are IDHmut and 44 are GBM. Samples were diagnosed and reclassified according to the WHO CNS 2021 criteria by expert pathologists. The second cohort, a control group referred to as the healthy cohort, consists of cortical tissue samples from 20 healthy individuals. Only patients without any history of cerebral damage or neurodegenerative diseases were included. In addition, comprehensive clinical and pathological data were collected for all patients, including sex, histological type, treatment, recurrence, and survival status. Tissue samples were collected following the patient's written informed consent and with the approval of the Ethics Committee of Hospital Universitario 12 de Octubre (CEI: 21/551 and 24/084).

2.2. Histological staining

The tissues were fixed at 4 °C in 4% formaldehyde, dehydrated in an ethanol gradient, before embedding in paraffin. The paraffin-embedded tumors were sectioned with a microtome (Leica Microsystems, Wetzlar, Germany) into slices of 3 μm, deparaffinized at 60 °C, and rehydrated with xylene and a decreasing gradient of ethanol, leaving them ready for subsequent staining. For this work H&E staining and diaminobenzidine (DAB) staining were used:

- **H&E:** H&E staining was necessary for the evaluation of tissue architecture, in addition to the identification of cellular structures [29]. The rehydrated tissue slides were submerged for 10 min in hematoxylin dye, staining the nucleus and ribosome rich regions in deep blue-purple. The tissues were then immersed in eosin dye for 30 s, staining the cytoplasm, collagen, and connective tissue in pink. Between the two steps, tissues were immersed in H_2O for 5 min to remove the remaining staining.

Table 1. Summary of clinical outcomes in the cohorts analyzed in this study. KPS stands for Karnofsky performance status, IDH for Isocitrate dehydrogenase and MGMT for O6-methylguanine-DNA methyltransferase.

Patient characteristics	Tumor cohort	Healthy cohort
Cohort size:	$n = 62$	$n = 20$
Median age (years):	55 (21–81)	54 (18–78)
Median KPS (range):	86 (70–100)	—
Sex:		
Female	25 (40%)	8 (40%)
Male	37 (60%)	12 (60%)
Extent resection:		
Total resection	39 (63%)	—
Subtotal resection	23 (37%)	—
Histological grade:		
Healthy brain cortex	—	20 (100%)
Astrocytoma IDHmut grade 4	18 (29%)	—
GBM IDHwt	44 (71%)	—
Molecular status:		
IDHmut	18 (29%)	—
MGMT methylated	24 (39%)	—
Treatment:		
STUPP protocol	53 (85%)	—

- **DAB:** DAB was used for the detection of specific proteins and molecular characterization of the tumors. After rehydration, for antigen retrieval, sections were treated using pressure cooking at 10 mM TRIS-EDTA pH 9.0. Permeabilized with 1% Triton X-100 (Sigma-Aldrich, St. Louis, USA) in PBS and blocked for one hour with a solution containing 10% FBS (Sigma-Aldrich, St. Louis, USA), 5% BSA (Sigma-Aldrich, St. Louis, USA) and 0.1% Triton X-100 (Sigma-Aldrich, St. Louis, USA). Tissues were incubated overnight at 4 °C with the anti-IDH1 R132H primary antibody (H09;1:200;Dianova,Hamburg,Germany). The next day, the slides were washed three times with PBS X-1 (Nzytech, Lisbon, Portugal) and incubated with biotinylated secondary antibody (1:200). For target protein detection, the ABC kit and DAB solution (Vector Laboratories, Newark, CA, USA) were used. This method will be further used for methodology validation, as presented in the section 3.4.

2.3. Image acquisition

The database used in this work has been captured using an Olympus BX-51 brightfield microscope (Olympus, Tokyo, Japan) equipped with a Basler ace acA5472-17uc RGB camera (Basler, Ahrensburg, Germany), a motorized stage *X–Y* Prior H101BXDK (Prior Scientific Instruments, Fulbourn, Cambridge, United Kingdom), and a 100 W halogen bulb (Phillips, Amsterdam, The Netherlands). This entire system allows automatic capture thanks to a firmware and capture software designed and developed by the authors. The details of this system are described in our previous work [30], along with a capture methodology developed to automatically capture images in areas of high interest marked by a pathologist figure 4. For the reader's convenience, a brief summary of this methodology is provided:

- Once the sample has been prepared using the technique described in section 2.2, a WSI of the sample with a 4× magnification is captured. Noteworthy, the tissue block used in this study was not arbitrarily selected; rather, it was part of a routine diagnostic workflow in which the entire block underwent comprehensive histological and molecular evaluation by the pathology department to ensure accurate tumor identification and characterization. After this initial assessment, a representative H&E-stained section was selected for annotation and its corresponding WSI capture.
- These WSIs are subsequently loaded into specific software developed by the authors at [30] that allows expert pathologists to analyze the image in detail. From their assessments, they can mark regions of interest (by highlighting them with rectangles of variable size). Such regions of interest may belong to: tumoral regions, non-tumoral regions, healthy regions, different types of vessels and necrosis, peripheral areas and edemas.
- This marking process generates a file with all the coordinates that later are read back by the capture software, which allows capturing these regions at the magnification desired for the study. It is

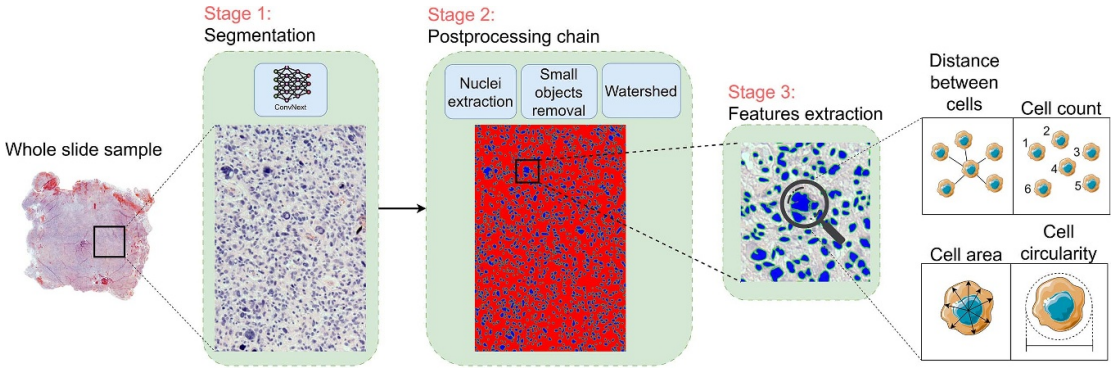

Figure 1. Diagram of the entire processing chain. The process begins with a whole slide image scanned at 4× magnification, where the pathologist marks the areas of interest. Each area is then automatically captured at 10× magnification. In Stages 1 and 2, cells within the image are detected, segmented, and refined to generate a segmentation mask. In Stage 3, morphological features are extracted from the segmented cells, including intercellular distance, cell area, circularity, and cell count.

important to note that the captured images will always be in optimal focus thanks to the auto-focus algorithm developed in [30] and the subsequent review of the images by the microscope operator.

It is important to note that, in contrast to other state-of-the-art studies, the images used in the present work were acquired at a 10× magnification. The decision of using the 10× magnification was to enable the evaluation of tissue architecture, particularly spatial features such as intercellular distance and cell distribution. This magnification provides a sufficiently wide field of view to capture hundreds of cells per image, improving statistical power and spatial context. While it does not resolve subnuclear details, the general morphology needed for our analysis remains clearly discernible. This balance makes 10× optimal for assessing the tumor microenvironment in a spatially informed manner.

This is why the images captured in the database have a pixel size of 0.24 μm/pixel and a resolution of 3672 × 5496 pixels. The exposure time for capturing at 10× is 11 ms with an automatic white balance performed internally in the camera.

2.4. Processing chain

This work proposes a diagnosis assistant tool based on DL, as outlined throughout this section and illustrated in figure 1. Starting from the images acquired as described in the previous section, a cell segmentation process is performed (figure 1—Stage 1), followed by a post-processing step to refine the results (figure 1—Stage 2). From this segmentation, the morphological features of each individual cell are extracted (figure 1—Stage 3), which are then used to perform a classification step, ultimately constructing the proposed diagnosis assistant tool.

2.4.1. DL-based cell segmentation module

One of the main challenges to be addressed in this work is to correctly segment the cells in the images as accurately as possible, in order to extract their morphological features using it for a successive stage to classify the slice in the diagnosis assistant tool. Following the conclusions of the reviews analyzed in section 1, as well as the current trends in generic semantic segmentation, several CNNs were tested: U-Net [31] in its default version, DeepLabV3 [32], and DeepLabV3+ [33] using ResNet-50 and ResNet-101 in both networks as backbones. All these networks are convolutional models based on the encoder–decoder pattern, which allows an extraction of the fundamental information of the image by means of dimensional reduction in successive layers (encoding) to later reconstruct it based on this fundamental information (decoding). When tested, they tend to cluster cells that are relatively close to each other rather than individually segment them. For this reason, ConvNeXt [28] was also tested. Although this network belongs to the CNN family, its internal architecture is based on visual transformers [34]. It incorporates a disruptive architecture along with recent normalization and optimization techniques like larger kernel sizes, GELU activation function instead of ReLU, and layer normalization; representing a significant evolutionary leap compared to the models mentioned above. In particular, the ConvNeXt-XL configuration was chosen with the backbone trained using the ImageNet-21k dataset [35] with 640 × 640 pixel crops. This configuration allows the network to observe more cells per crop, greatly improving the metrics of the segmentation with respect to smaller crops. For convenience, the

Table 2. Summary of the dataset used for the fine-tuning training of the CNNs. The patients selected are as representative as possible and to avoid bias each crop only belongs only to one of the sets.

Dataset	Class	Number of patients	Number of 640 × 640 crops
Training set	Tumor	6	324
	Healthy	9	486
	TOTAL	**15**	**810 (75%)**
Validation set	Tumor	1	54
	Healthy	1	54
	TOTAL	**2**	**108 (10%)**
Test set	Tumor	1	54
	Healthy	2	108
	TOTAL	**3**	**162 (15%)**

open source OpenMMLab framework, MMSegmentation [36], has been used to develop the training experiments.

As in any custom re-training process of a neural network for semantic segmentation, it is necessary to generate proprietary ground-truth masks to enable the network to learn the specific features of the images being used. Consequently, the ground-truth labeling process involved selecting 20 representative images from different patients and precisely annotating the position of each cell. To balance the number of cells from tumor and healthy tissue images, 8 out of the 20 selected images were from tumor tissue, while the remaining 12 were from healthy tissue. QuPath 5.0.0 [37] was the tool chosen to annotate the nuclei of each cell by an expert pathologist. After the pathologist annotated the images and the ground-truth masks were generated, two other pathologists performed a review and correction process to normalize the interoperability error. A total of 51 228 cells were labeled. Following the idea presented by Salvi *et al* [38], three classes have been used to label the images: background, nuclei, and border. The use of a border class as an auxiliary class for delimiting each nuclei is implemented to improve the separation of fusion cells in a postprocessing stage after segmentation. Pathologists only annotated the nuclei pixels, while the borders were geometrically calculated using image morphological transformations as a dilation operation of 3 pixels. In the border class creation method proposed by Salvi *et al* a 5 pixel dilation was used due to the higher magnification of their microscope, which resulted in lower cell density per image. Since the images of the presented database show more densely packed cells at lower magnification, we used a 3 pixel dilation to preserve useful pixels in the nuclei class. The background class was defined as all remaining pixels that did not belong to the nucleus or the border. Therefore, the final ground-truth mask consisted of pixels with a value of 0 for the background, 1 for the border, and 2 for the nucleus. Therefore, the result of the labeling procedure is a mask with the same resolution of the input image that is then split into patches of 640 × 640 pixels with 33 pixels of overlap to match the image size used during the ImageNet-21k backbone training. In order to demonstrate the empirical usefulness of the border class, the results of the segmentation experiments without the border class are attached in section 3 of the supplementary material.

The entire dataset used for fine-tuning training the networks is summarized in table 2. Train, validation and test splits have been carried out at patient level to prevent patient-leakage (cross-referenced data between the splits). The sets are class-stratified to avoid imbalance between cells for each crop, thus preventing bias in training. Each crop from a given patient appears in only one of the three sets, preventing overlap and minimizing bias. To obtain the best performance, a hyperparameter optimization process has been conducted. The ranges of values tested for each hyperparameter together with their final value are summarized in table 3. The loss function applied was cross-entropy weighted [39] where the weights of each class are set to balance the classes, the balance of pixels per class being 87.8% of the pixels for background, 3.79% for the border class and 8.43% for nuclei. To improve the variability of network training data, several data augmentation techniques were applied to the training set: random horizontal and vertical flip, random rotation with a range of 45° to −45° and CLAHE contrast, each with a probability 50%. The training process took 120 min on a dedicated server with a Nvidia A100 80GB, 2× AMD EPYC 7317 16-Core Processor with 64 threads, and 1TB of RAM. For the readers' convenience, a table detailing the versions of all components used in the presented work is provided in the supplementary material to ensure the repeatability of the experiments.

Table 3. Values used during the hyperparameters optimization of the ConvNeXt -XL network and its results.

Hyperparameter	Range/values	Final value
Learning rate	$[x \times 10^{-}i \mid x \in [1:9],\ i \in [2:6]]$	2×10^{-5}
Batch size	[4, 8, 12, 16, 20]	8
Epochs	[20:200]	60
Crop size	[256 × 256, 512 × 512, 640 × 640]	640×640

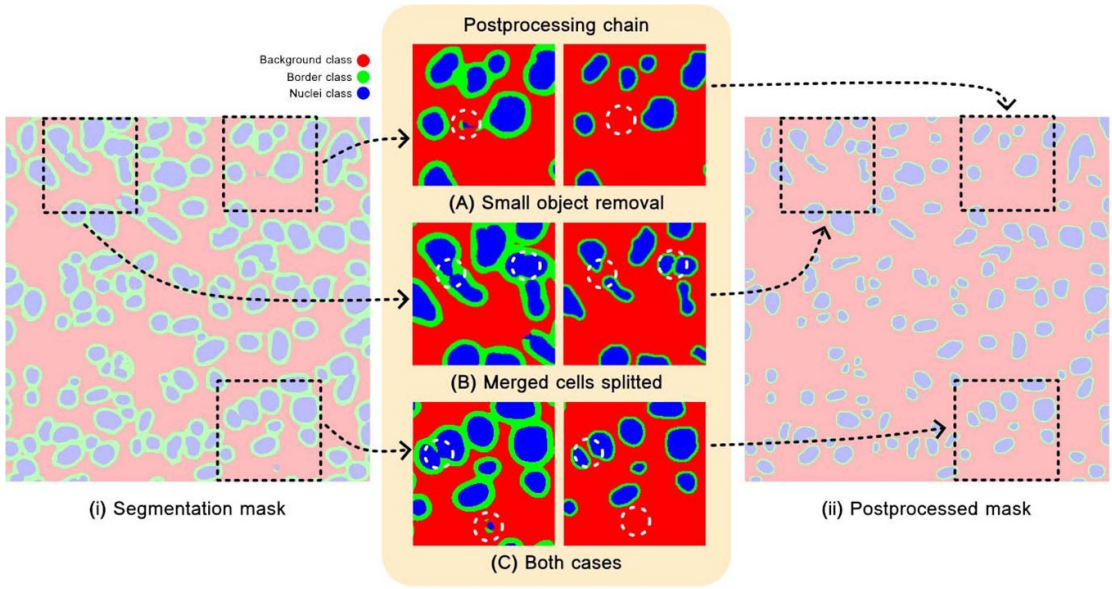

Figure 2. Example of operation of the postprocessing stage. On the left (i) is the segmentation mask, coming directly from the neural network output. It shows erroneously fused cells, incongruent edges and small errors in the segmentation. After the post-processing stage, on the right side (ii) is the the postprocessed mask. On this mask, small errors are eliminated, wrong fused cells are separated and the edges are homogenized.

2.4.2. Postprocessing

In order to reduce the noise and imperfections in the detected instances from the segmentation, a post-processing stage is necessary. In the case of cell segmentation, these imperfections generally come from the detection of cells that are in a fusion stage but still have two nuclei. To minimize these errors, a modified version of the postprocessing chain presented by Salvi *et al* [38] is implemented (figure 2). The process starts at the final layer of ConvNeXt, where it generates a softmax probability map that it is converted to a segmentation mask by selecting in each pixel the class with the highest probability (figure 2(i)). In consequence, the mask contains pixels corresponding to the classes background (0), border (1) and nuclei (2). From this segmentation mask, a submask is generated only with the pixels corresponding to the nuclei class where, applying the method *findContours* of the OpenCV [40] library, its contours are extracted. The contours with an area less than 20% of the global mean area of the image are then discarded (figure 2(A)) according to the methodology proposed in [38]. Next, a marker-based watershed segmentation is applied to split the cells that were initially detected as merged (figure 2(B)). The final step is a dilation morphology operation with a 3 pixel radius to set again the border class completely normalized (figure 2(i)).

2.4.3. Features extraction

After the images have been processed by the segmentation module and the post-processing stage, a methodology is developed to extract morphological features from these segmentation masks. This methodology allows to extract the distance between neighboring cells from an image, which provides a context of cell density regardless of whether this tissue has broken or empty areas. It also extracts the number of cells in the image, i.e. the cellularity as well as the circularity and area of each cell.

To do this, a submask is first generated with only the pixels belonging to the nuclei. From them, the external contours of each of the nuclei are detected using the method *findContours* from the OpenCV library and also its centroids are calculated. The distance between neighboring cells is calculated by applying the Nfinder tool developed by Moretti *et al* [41]. To use this tool, the calculated centroids must

Table 4. Summary of the dataset used for training and testing of the Diagnosis assistant tool.

Dataset	Number of patients
Training set	74 (55 tumoral 17 healthy)
Test set	9 (7 tumoral 3 healthy)

be provided as input. Based on these centroids, a Delaunay triangulation is applied to establish connections between them. Subsequently, a set of trigonometric rules based on the angles formed by these connections is used to distinguish between adjacent and distant cells. In this way, only the distances between neighboring cells are obtained. As for the rest of the features, the number of cells is directly the number of instances, the circularity is calculated by extracting the parameter of the detected contour applying equation (1) and the area is calculated by OpenCV with the *contourArea* function,

$$\text{circularity} = \frac{4\pi \times \text{area}}{\text{perimeter}^2}. \tag{1}$$

2.4.4. Diagnosis assistant tool

Throughout this section, it has been presented how the images from the database have been captured, how the cells from those images have been segmented by a custom-trained ConvNeXt CNN and how the features from those segmentations have been calculated. This information provides pathologists with fundamental insights to help them improve diagnostic accuracy. One of the contributions of this work is the development of a diagnosis assistant tool based on the classification of the extracted features that allows determining whether an image is tumoral or healthy. This type of aid tool helps pathologists in the diagnostic process, since it allows a first screening. Indeed, it can also help improving the diagnosis by reducing the interobserver variability. In addition, the workload of the hospital pathology department could be considerably reduced.

The assistant tool presented consists of an image classifier based on the processing of the extracted features once the images have been segmented. To do that, a RF model [42] was trained taking into account all images in the database, segmenting them and extracting their features. As explained in section 2.1, each of the images in the database is extracted from a specific tissue region from a specific patient, whose precise diagnosis is known. This is why the labels of all the images can be immediately inferred, generating the ground truth for training the algorithm. The values of these labels are 0 for images corresponding to patients with healthy tissue and 1 for images from patients with tumor tissue.

The training process consists of performing a RF with 100 estimators. Due to the limited number of healthy patients, the dataset is imbalanced, with 757 images of tumoral areas and 800 images of healthy areas. To address this imbalance, an additional 10-fold cross-validation is applied, where an equal number of images are randomly selected from each class to match the number of samples in the minority class. Additionally, as RF is a decision tree-based classifier, it allows the interpretation of feature importance in the classification task. All classification metrics and feature importance scores are averaged across the k-fold iterations to obtain robust performance estimates. The patients summary is listed in table 4.

2.4.5. Statistic analysis

GraphPad Prism on version 8.0.2 was used for patient-level statistical data analysis.The primary used statistical test was the Mann–Whitney test. However, the appropriate statistical test was carefully chosen for each analysis, considering the variance and distribution of the data. The Shapiro–Wilk test was used to assess normality and determine whether a parametric or nonparametric test was appropriate. The nonparametric Mann–Whitney test was applied when the data did not follow a normal distribution. For normally distributed data, homogeneity of variances was assessed: Student's t-test was used for equal variances, and Welch's t-test was performed when variances were unequal for variance inequality correction. To enhance the robustness and interpretability of the results, the mean and standard error of the mean (SEM) were computed for each group, and 95% confidence intervals (CI 95%) were calculated.

3. Results

This section details the results of each of the parts described above, with a workflow highlighting main steps of the process (figure 3). Starting with biopsy collection and sample handling, continuing with data acquisition and finishing with data analysis.

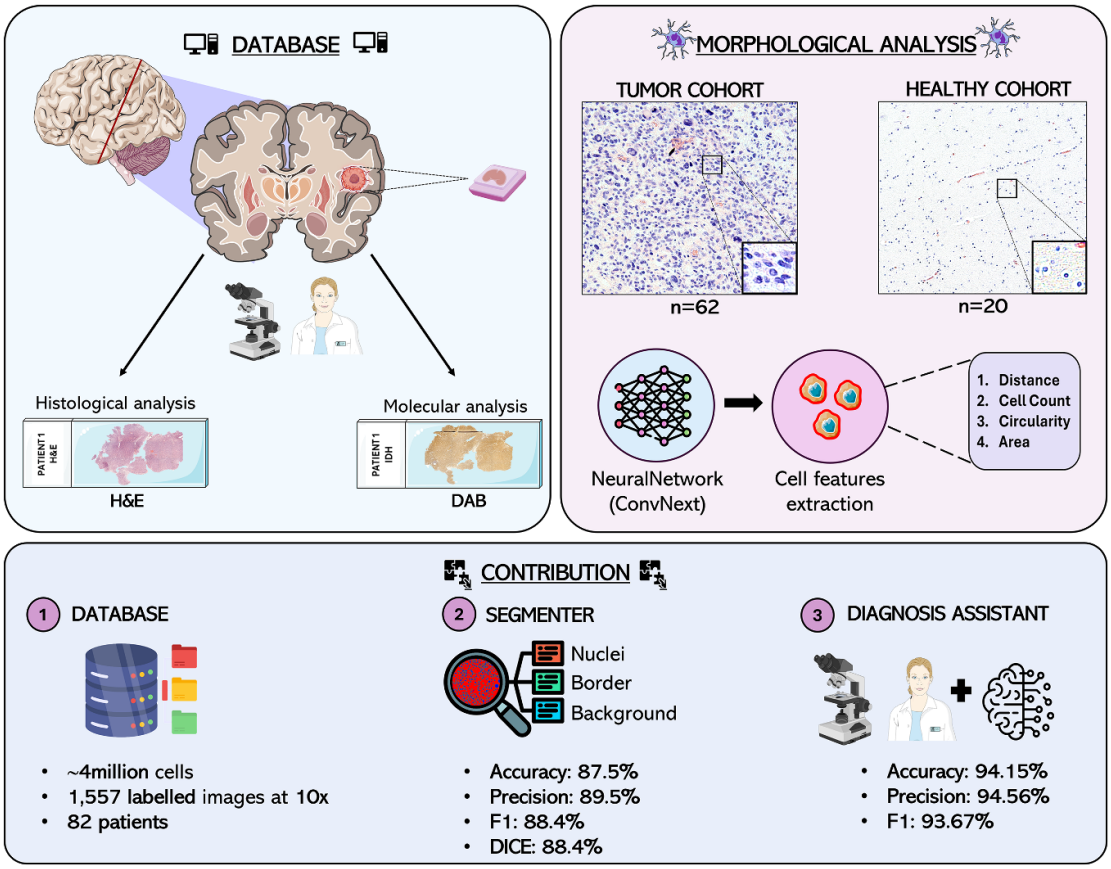

Figure 3. Workflow illustrating the key aspects of this research. Large database sample management (top-left), segmentation using a neural network and extraction of cell morphological features (top-right), and the main contribution of this work (bottom).

3.1. Database

The database comprises biopsy samples from 82 patients, including representative images of both tumor and healthy tissue obtained during routine high-grade astrocytoma diagnostics. All samples were selected from validated retrospective cohorts by expert pathologists and include grade 4 IDHmut astrocytomas ($n = 18$), GBM ($n = 44$), and healthy patients as control ($n = 20$). Data were captured according to the protocol described in our previous work [30]. For each patient, WSI was scanned and subsequently labeled by the pathologist with the aim of capturing them in detail as described in section 2.3. From these highlighted regions, a total of 2651 RGB images were collected. For this work, a total of 1557 images at 10× magnification were used, while the remaining ones, corresponding to the tumor microenvironment, will be used for future studies. The distribution of the images in this work is as follows: 800 images corresponding to healthy tissue, 757 belonging to the different tumor core regions, representing intratumoral heterogeneity (figure 4). Furthermore, morphological information was extracted from 4123 440 cells, ensuring a high degree of heterogeneity, which is statistically beneficial for obtaining more robust and generalizable results.

3.2. Cell segmentation module performance metrics

To analyze the performance of the cell segmentation module along with the postprocessing chain, a series of metrics have been obtained on the test set. For reader convenience, only the two best results in terms of performance on the test dataset are shown, which are equivalent to ConvNeXt XL and Deeplav3+ with ResNet-101, both trained with a crop size of 640 × 640 pixels. The evaluation includes both pixel-level and region-based metrics. At pixel level, precision, accuracy, recall, and $F1$ score were used. For region-based analysis, the DSC was computed. The results are presented in table 5. The metrics have been obtained for the background, nuclei and border classes. However, the results of the border class have not been taken into account from the average metric calculation because it is an auxiliary class that is taken into account only to improve the split between merged cells in the postprocessing stage, as explained in section 2.4.2.

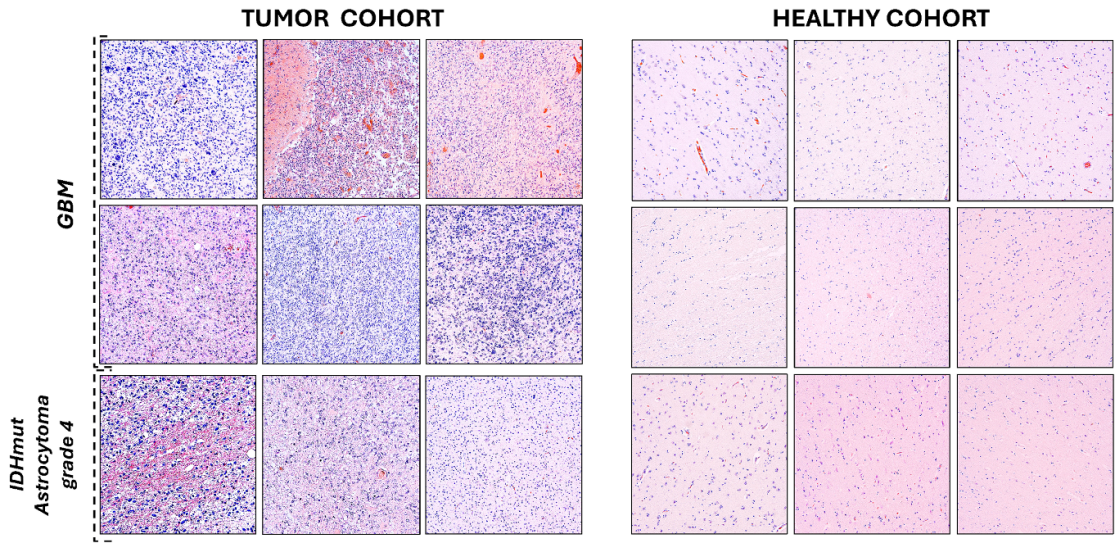

Figure 4. Representative H&E images of the cohort heterogeneity. Tumor cohort (left), and healthy cohort (right), captured with custom setup [30].

Table 5. Summary of the metrics obtained in the test dataset by DeepLabV3+ R-101 and ConvNeXt XL. The average is calculated without taking into account the auxiliary border class.

		Pixel-based metrics				Region-based metrics
Network	Classes	Precision	Accuracy	Recall	*F*1 score	DICE
DeepLabV3+	Background	97.2%	96.3%	96.3%	96.8%	96.8%
	Border	29.5%	49.4%	49.4%	37.1%	37.1%
	Nuclei	80.4%	65.3%	65.3%	72.1%	72.1%
	Average	88.8%	80.8%	80.8%	84.8%	84.4%
ConvNeXt	Background	99.6%	90.6%	90.6%	94.9%	94.9%
	Border	22.0%	67.6%	67.6%	33.2%	33.2%
	Nuclei	79.4%	84.5%	84.5%	81.8%	82.1%
	Average	89.5%	87.5%	87.5%	88.4%	88.4%

Table 6. Summary of the average and SEM of morphological metrics. Obtained in the morphological analysis of both cohorts, tumor (left) and healthy (right).

	Tumor cohort		Healthy cohort		
Feature	Mean ± SEM	CI 95%	Mean ± SEM	CI 95%	p-value
Cell distance	$20.90 \pm 0.6594\ \mu m$	19.58–22.22 μm	$36.06 \pm 0.8323\ \mu m$	34.32–37.80 μm	$p \leqslant 0.0001$
Cell count	3839 ± 194.6	3450–4228	1194 ± 54.28	1081–1308	$p \leqslant 0.0001$
Cell circularity	0.745 ± 0.0036	0.737–0.752	0.816 ± 0.0018	0.812–0.819	$p \leqslant 0.0001$
Cell area	$297.3 \pm 5.382\ \mu m^{-2}$	286.5–308 μm^{-2}	$217.7 \pm 3.225\ \mu m^{-2}$	210.9–224.4 μm^{-2}	$p \leqslant 0.0001$

3.3. Morphological analysis

The plasticity displayed by tumor cells highlights their ability to adapt to the response to stimuli from the microenvironment, which is part of the hallmark of aggressive cancers such as GBM [14]. These alterations involve modification of the cytoskeleton that affects the shape of the cells, how they move and interact with the microenvironment and have become a hallmark of malignancy, providing valuable information to distinguish tumor cells from healthy ones. Based on this premise, the cell segmentation module was employed to extract quantitative data (table 6) allowing numerical characterization of tissue and cell morphological changes such as distance between neighbor cells, cell count, area and circularity (figure 5).

- **Distance**: A significant difference in distance between cells was observed when the two groups were analyzed. Those with pathological tissue exhibited a lower distance between cells with an average of 20.90 μm compared to healthy tissue, which showed an average distance of 36.06 μm (figure 5(A)),

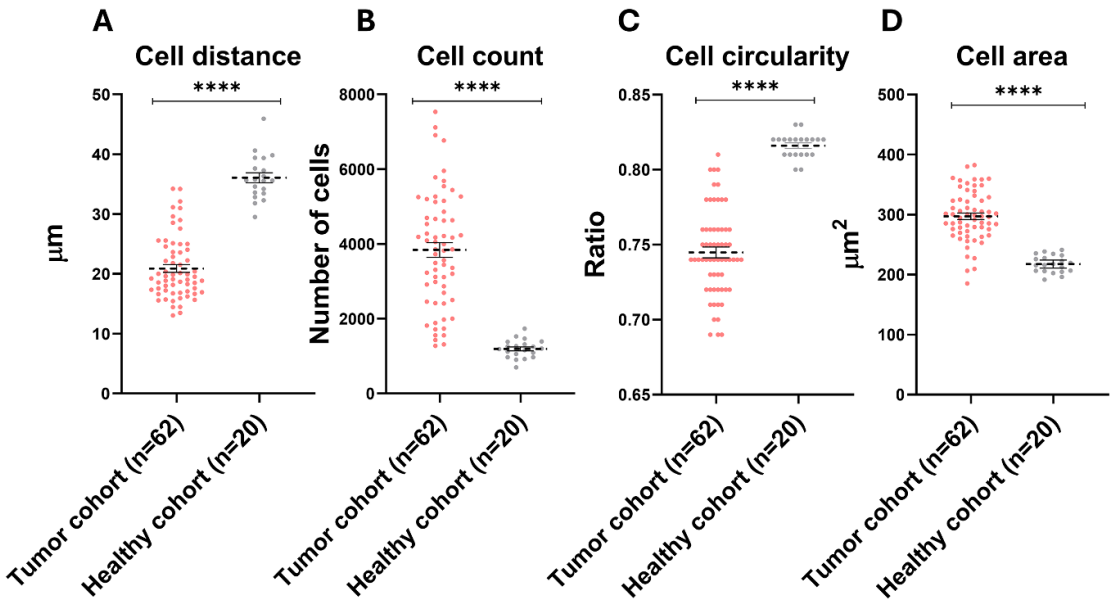

Figure 5. Tumor cells exhibit distinct morphological features compared to healthy ones. Violin plots comparing morphological features between tumor ($n = 62$) and healthy cells ($n = 10$): cell distance (A), cell count (B), cell circularity (C), and cell area (D). The significance of morphological features were analyzed using a Student's t-test and Mann–Whitney test. $p \leqslant 0.05$ (*), $p \leqslant 0.01$ (**), $p \leqslant 0.001$ (***), $p \leqslant 0.0001$ (****). n.s., not significant.

highlighting this difference as a potential morphological marker for tumor identification and indicator of tumor proliferation.

- **Cell count**: Tumors are defined as abnormal and rapid cell growth. Precisely, that is exactly one of the key features used for tumor diagnosis, cell density. In our study, it was found that tumor tissues contain approximately 3.22 times more cells in average than healthy tissues. These findings are entirely consistent with the previously obtained data. When cell count increases, the distance between neighboring cells decreases in tumor tissue (figure 5(B)).
- **Circularity**: Regarding the cell morphological characteristics assessed within this cohort, the findings showed that tumor cells in diseased patients exhibited not only a notable increase in cellular density, but also a diminished circularity, with an average value of 0.745 in tumor tissue compared to 0.816 for healthy tissues. It is noteworthy that circularity, measured on a scale from 1 to 0, signifies a perfect circle at 1 and a 0 a flat line (figure 5(C)).
- **Area**: Moreover, regarding area analysis, it was observed that those cells, presenting a progressive loss of circularity, were the same that showed a higher area, 297.3 μm^{-2}, compared to control tissue cells with a value of 217.7 μm^{-2} (figure 5(D)) .

These results align with well-established and previously mentioned concepts in oncologic literature [43]. In solid tumors, cells density increases as tumor grows, leading to the loss of normal tissue architecture. This is manifested by significant variations in progressive morphological changes such as intercellular distance [10], resulting from uncontrolled growth, loss of cell polarity, and matrix remodeling [44]. However, although these changes are widely recognized in the field, they have not yet been precisely quantified or objectively established into diagnostic criteria. In cancer, the deregulation of the cell cycle and increased nuclear pleomorphism contribute to a larger cellular and nuclear size [13, 45]. Indeed our results showed significant loss of cellular circularity, with tumor cells adopting flatter and more irregular shapes. The observed flattening and increased area of tumor cells can be attributed to several interconnected biological mechanisms. Additionally, the loss of cell polarity and reduced adhesion between neighboring cells due to their change towards a more mesenchymal phenotype alters the balance between cell-cell adhesion, extracellular matrix tension, and the restriction of proliferation through inhibitory contact affecting on the cell distribution [15], which disrupts the structural constraints that healthy tissues present. Furthermore, the physical separation between the nuclei or membranes of adjacent cells, usually measured in micrometers using digital histomorphometric analysis, is exacerbated by the mechanical stress generated by rapid tumor growth, which causes cellular overcrowding and reduces the space between cells. This phenomenon leads to displacement of surrounding tissue structures and, consequently, sustaining tumor growth and invasion [46] underscoring one of the major issues in brain

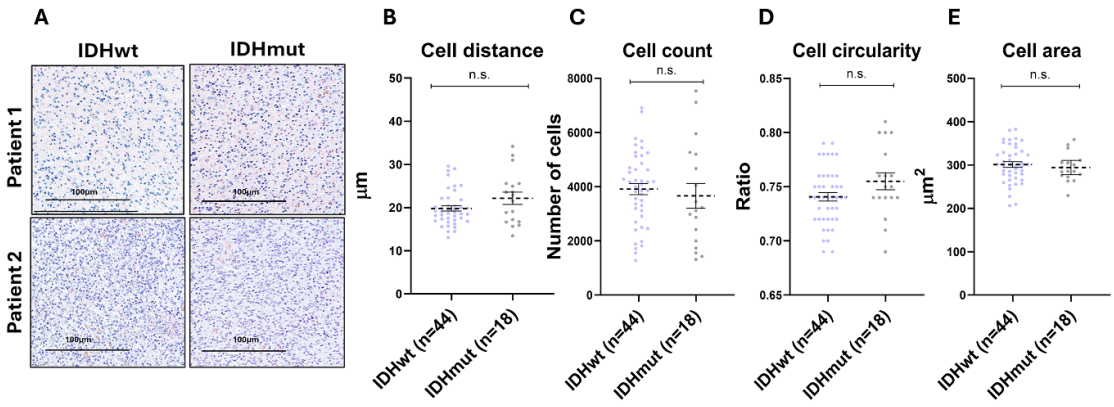

Figure 6. IDHwt and IDHmut patient present similar tumor cell morphological features. Violin plots comparing morphological features between IDHwt ($n = 44$) and IDHmut ($n = 18$): cell distance (a), cell count (b), cell circularity (c), and cell area (D). The significance of morphological features were analyzed using a Student's t-test and Mann–Whitney test. $p \leqslant 0.05$ (*), $p \leqslant 0.01$ (**), $p \leqslant 0.001$ (***), $p \leqslant 0.0001$ (****). n.s., not significant.

tumors, which generates alteration of cerebral functions. This results in physical and cognitive impairments experienced by patients which impact negatively in their quality of life [47, 48]. In contrast, healthy tissue is characterized for maintaining an organized and relatively constant arrangement in terms of cell morphology and intracellular distance, which is associated with tissue homeostasis and the functionality of the extracellular microenvironment [43].

Therefore, intracellular distance reflects the architectural organization of the tissue, and its alteration serves as a key indicator of pathological processes such as tumorigenesis.

3.4. Validation experiment

As mentioned in the introduction, one of the main parameters to determine the aggressiveness of a tumor and classify it correctly, besides morphology, is the use of molecular analyses such as the presence of the IDHmut.

Tumors with IDH mutations are typically classified as grade 2 or 3 astrocytomas. These are characterized by the absence of necrosis, vascular proliferation, and a lower mitotic index, and they tend to exhibit less aggressive behavior. However, a small subset which represents approximately the 10% of cases display histological features similar to GBM, indeed they present characteristics such as high necrosis and vascular proliferation (figure 6(A)), that is precisely why these tumors are classified as grade 4 IDHmut astrocytomas [3]. Our cohort is specifically composed of GBM and grade 4 IDHmut astrocytomas. Noteworthy, pathologists are unable to distinguish these tumors based exclusively on tissue architecture and cell morphological features. Since our main objective is to classify grade 4 astrocytomas regardless of their molecular profile, the first step was to verify our tool robustness and verify that patients did not differ in the proposed morphological parameters when grouped by molecular characteristics. The cohort was stratified into IDHwt ($n = 44$) and IDHmut ($n = 18$) groups (figure 6(A)). Results showed no statistically significant morphological differences between the IDHwt and IDHmut groups (figures 6(A)–(E)). However, cells in the IDHmut group showed a subtle tendency toward a less tumor-like tissue architecture and morphology, reflected in a lower cell density, with an average of 300 fewer cells per tissue sample, indicating a less crowded tumoral tissue. This difference was also evident in the spatial arrangement of the cells, which were, on average, 2 μm farther apart compared to the GBM tissues. At the cellular morphology level, IDHmut cells exhibited a more rounded shape, with this feature showing the most pronounced statistical trend. This observation is consistent with classical histological (H&E) analysis, in which IDHmut grade 4 astrocytomas and IDHwt GBMs present similar cellular profiles and only minor survival differences. Notably, this also highlights the strength of our tool, as it is capable of detecting even subtle morphological trends.

To validate the obtained data from the morphological characterization of tumor cells and the robustness of the presented methodology, an analysis of peripheral tumor tissue was performed in H&E slide and validated molecularly by employing IDHmut marker on a contiguous tissue slide. During surgery, the resection extends beyond the tumor core to include distal marginal areas where tumor cells infiltrate parenchyma. The presence of diffuse glioma infiltration in these regions plays a key role in pathological diagnosis (figure 7(A)). For this validation we used an external validation cohort of 10 patients that were not part of our initial tumor cohort. This cohort is composed of 152 images exclusively of tumor tissue,

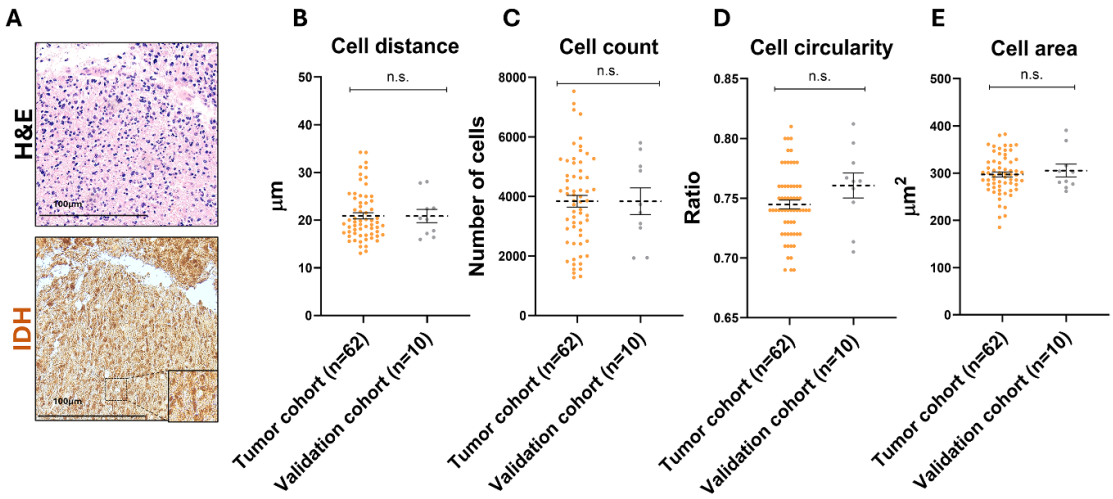

Figure 7. Validation of metrics in a peripheral cohort. Violin plots comparing morphological features between tumor cohort ($n = 62$) and validation cohort ($n = 10$): cell distance (a), cell count (b), cell circularity (c), and cell area (D). The significance of morphological features were analyzed using a Student's t-test and Mann–Whitney test. $p \leqslant 0.05$ (*), $p \leqslant 0.01$ (**), $p \leqslant 0.001$ (***), $p \leqslant 0.0001$ (****). n.s., not significant.

Table 7. Summary of the average metrics and SEM obtained in the validation experiment.

	Tumor cohort		Validation cohort		
Feature	Mean ± SEM	CI 95%	Mean ± SEM	CI 95%	p-value
Cell distance	$20.90 \pm 0.6594\ \mu$m	19.58–22.22 μm	$20.85 \pm 1.386\ \mu$m	17.72–23.99 μm	0.8286
Cell count	3839 ± 194.6	3450–4228	3836 ± 447.8	2823–4849	0.9955
Cell circularity	0.745 ± 0.0036	0.737–0.752	0.760 ± 0.0104	0.737–0.784	0.117
Cell area	$297.3 \pm 5.382\ \mu m^{-2}$	286.5–308 μm^{-2}	$305.3 \pm 13.57\ \mu m^{-2}$	274.6–336 μm^{-2}	0.5806

Table 8. Summary of the classification aid tool metrics obtained from the test dataset of feature extractions generated by DeepLabV3+ R-101 and ConvNeXt XL.

	Classification metrics				Variable importance			
Network	Precision	Accuracy	Recall	$F1$ score	Distance	Cell count	Circularity	Area
DeepLabV3+	93.55%	92.62%	90.16%	91.46%	36.30%	28.22%	26.50%	8.98%
ConvNeXt	94.56%	94.15%	93.55%	93.67%	39.73%	33.94%	18.50%	7.82%

captured under the same capture conditions as the primary cohort (table 1). To capture the images, the already presented protocol of whole slide scanning, labeling by pathologist zones and subsequent capture of these zones at 10× was followed under the same conditions. Subsequently, cell segmentation of each image was performed and morphological analysis was performed. (figures 7(B)–(E)).

When comparing the validation results with those obtained from the primary cohort, it was observed that the morphological metrics (intercellular distance, area, circularity, and cellularity) remained within the expected variability range, with no significant differences $p > 0.05$ (table 7).

Together, these results confirm the robustness of the proposed approach, demonstrating that the cell metrics obtained from the tumor tissue are consistent with the extracted and validated data.

3.5. Diagnosis assistant tool metrics

Finally, the metrics resulting from the diagnosis assistant tool are presented (table 8). The precision, accuracy, recall, and $F1$ score of the test dataset have been measured. In addition, the importance of the variables obtained as the weights extracted from each of the 50 estimators used in this RF configuration have been incorporated. In addition, we implemented an end-to-end binary classification baseline and computed extended evaluation metrics to compare it with the proposed multistage approach. Although the end-to-end model yields slightly improved performance in some metrics, it lacks interpretability due to the absence of intermediate parameters relevant for biological analysis later described. These complementary results are provided in the supplementary material to preserve the manuscript's focus.

4. Discussion

Despite advances in GBM diagnosis, this tumor remains a challenge due to its high recurrence rate, occurring in 95% of cases. This recurrence arises from the presence of infiltrating tumor cells at the periphery of the tumor, which cannot be detected even with advanced magnetic resonance imaging studies. Furthermore, tumor margin areas are difficult to distinguish during both surgery and intra-operative histopathological analysis. The high heterogeneity of GBM leads to interpretative variability among pathologists, making the standardization of the diagnostic process a challenge. In response, DL-based systems are increasingly being implemented in digitized pathology departments worldwide to support diagnostic efforts. These systems not only enables to standardize the diagnostic process [49, 50], but also can help with the prediction of the disease prediction [51–53]. However, other research groups have tried to study and generate H&E image-based databases focused on the analysis of 40× image features rather than cellular characteristics [25, 54, 55]. For example, Cheung *et al* developed an AI system based on texture-image analysis, obtaining features such as contrast, dissimilarity, difference variance, entropy or energy among other features [55]. Only some, such as the one presented by Hou *et al* [56], are focused on cellular features, although they perform a superficial and generalized analysis presenting limited labeled data and a lack of in-depth morphological analysis. In fact,to the best of our knowledge, the limited prior studies have not created a large-scale numerical database of GBM cell morphology, which is essential for developing a DL-based diagnostic assistant tool.

Based on these considerations, this work presents a novel DL-based tool with the aim of assisting pathologists in performing an initial screening between tumoral and healthy tissue with high precision. The system automatically detects the cells from H&E 10× captured images and generates a segmentation mask thanks to a fine re-training of the CNN semantic segmenter ConvNeXt-XL. Moreover, the segmentation masks generated by the network are refined in a postprocessing stage where small imperfections are cleaned and cells, mistakenly detected as merged, are conveniently isolated. The combination of the semantic segmenter and the postprocessing stage is capable of distinguish between background and cell nuclei with an average precision of 89.55% and an average DICE of 88.4%. During the development, in addition to ConvNeXt, several CNN such as U-Net, DeepLabV3 and DeepLabV3+ were tested. However, the general behavior tendency of these networks was to detect large clusters of cells instead of making a much finer detection that would allow the segmentation of adjacent cells individually and thus not falsify the extracted morphological features. On the other hand, the great value of the ConvNeXt architecture chosen in this paper is that it allows a precise segmentation at the individual cellular level. For the re-training process, a reduced but convenient dataset of 540 640 × 640 pixels crops belonging to 10 characteristic patients was created in which each cell was manually labeled by 3 different pathologists to reduce interobserver variability. This allowed the network to learn in a precise manner according to the metrics generated from the evaluation of the test dataset (table 5) and a subjective and consistent evaluation of the expert pathologists on the predicted database.

Leveraging the segmenter's capability to detect and segment individual cells on tissue images, the next step of this work focuses on extracting the most representative morphological features: distance between neighboring cells, cell count, cell area, and circularity. Instead of directly analyzing image-level properties like previous studies, we have examined individual cells for a more detailed approach. To the best of authors' knowledge, distance between neighbor cell has not previously been used in the diagnosis of glioma. The data obtained revealed that tumor tissue cells gradually lose their regular structural and morphological characteristics. Specifically, the quantification of these features allowed us to conclude that tumor tissue contains 3.22 times more cells, which are 1.73 times closer together and exhibit an average area of 297.3 μm^{-2} and a circularity of 0.745.

The ability to extract these morphological features from the captured images has enabled the development of a diagnostic assistant tool that can discern between healthy and tumor images. This tool is based on the RF classification algorithm. Specifically, an RF with 100 estimators has been implemented together with a cross-validation based training approach with 10 k-folding and class balancing to reduce bias as much as possible. As a result, it was able to classify the morphological features extracted from the images with an accuracy of 94.15% and an $F1$ score of 93.67%. It is important to emphasize the deep relationship between the segmenter and the classifier. In fact, the results obtained by the segmentation module and the classifier shown in table 5, demonstrate that to maximize the performance of the diagnosis tool, it is crucial to maximize the performance metrics of the semantic segmentation. A more precise segmentation of individual cells enables more accurate morphological feature extraction, ultimately improving classification performance. The main advantage of using RF is the ability to statistically infer which variables have influenced the decision the most, otherwise hidden. In this work, it

is clearly observed that the distance between neighbor cells is the most influential parameter in the classification, with an influence over 35%, followed by the number of cells, the circularity of the cells, and the area of the cells. It is important to understand how cells are distributed and coordinated within parenchyma, as this is crucial for maintaining their proper function. Different studies have shown that the quantification of spatial parameters, including intercellular distance, provides valuable information on structural heterogeneity and the dynamics of cellular crowding [57–60]. For example, Gerdes *et al* (2013) applied multiplexed imaging to reconstruct cellular networks and demonstrated the importance of intercellular proximity in characterizing tumor microenvironments [57]. From a quantitative approach, intercellular distance has been proposed as an emerging biomarker to assess architectural disorganization and the degree of tumor aggressiveness. This tissue disarrangement has been explored in different cancers, including ductal carcinoma of the breast and gliomas. Yuan *et al* (2013) showed that metrics based on cellular topology, such as intercellular distance and nuclear connectivity, can discriminate between histological grades and predict recurrence in breast cancer [58]. Likewise, research in GBM has highlighted that the chaotic arrangement of tumor cells, with local gradients of crowding, is related to invasion patterns and therapy resistance [59]. The relevance of this metric expands when integrated with the biology of the tumor microenvironment, since intercellular distance can indirectly reflect variations in matrix stiffness, the presence of immune infiltrates, and modifications in contact-dependent signaling pathways [60]. Therefore, its quantification offers a complementary spatial descriptor to conventional morphological metrics (such as nuclear size or nucleus-cytoplasm ratio) and contributes to a more precise stratification of tumor phenotypes using AI and image analysis algorithms [58]. Thus, intercellular distance measurement constitutes a novel and biologically relevant parameter for the quantitative characterization of tissue architecture, capturing the complexity of crowding and disorganization inherent in neoplastic growth. Its incorporation into digital histopathology pipelines and clinical prediction models represents a step toward next-generation spatial histopathology.

In summary, the proposed system accurately segments cells from histopathological images captured at 10× magnification, extracts their morphological features and classifies tissue as tumor or healthy with 94.15% accuracy. We are aware that the full potential of this tool has not yet been exploited as it is not yet able to classify tumors according to their molecular characteristics. Nonetheless, the strong performance of both the segmenter and classifier, along with the high-quality data obtained in the database, represents a promising first step. In the future we aim to improve the presented tool by combining the presented advanced segmentation tools with hyperspectral imaging and molecular profiling, including transcriptomics and DNA methylation signatures, to improve glioma classification and diagnostic precision. This integrative approach is expected to enhance the accuracy and robustness of our analyses. This great potential makes us optimistic, as it paves the way for the continued development of brain tissue image-based diagnostic support tools based on morphological characteristics. In addition, we will test hybrid pipelines that allow to perform fast image classification based on end-to-end binary classifiers with a high accuracy while applying our multi-stage pipeline for detailed morphological analysis.

Data availability statement

The data cannot be made publicly available upon publication due to legal restrictions preventing unrestricted public distribution. The data that support the findings of this study are available upon reasonable request from the authors.

Acknowledgments

The authors acknowledge the technical and scientific assistance of Fernando Pescador, from Universidad Politécnica de Madrid, Kristen Mariko Meiburger, from Biolab, Department of Electronics and Telecommunications, Politecnico di Torino, Turin, Italy, and Berta Segura-Collar, from Hospital Universitario 12 de Octubre, Madrid, Spain. The samples were processed by Denisse Alcívar-López and Sandra Martín-Rodríguez, from Hospital Universitario 12 de Octubre, Madrid, Spain. The workflow was created with BioRender and Servier Medical Art.

Author contributions

Gonzalo Rosa-Olmeda, Sara Hiller-Vallina, Ricardo Gargini, and Miguel Chavarrías conceived the idea and methodology. Miguel Chavarrías and Ricardo Gargini supervised the project. Sara Hiller-Vallina and Ricardo Gargini prepared the samples, collected the data and labeled the datasets. Gonzalo Rosa-Olmeda,

Manuel Villa, Miguel Chavarrías and Massimo Salvi involved in investigation, formal analysis, and software. Gonzalo Rosa-Olmeda involved in data curation and visualization. Gonzalo Rosa-Olmeda and Sara Hiller-Vallina wrote the original draft. All authors reviewed and edited the final draft and approved the text.

Conflict of interest statement

The authors declare no conflict of interest.

Funding

This research was funded by the Spanish Ministry of Science and Innovation through the OASIS-RETIRO Project (PID2023-14 8285OB-C44), by the Instituto de Salud Carlos III (ISCIII) through the Projects: PI22/01 171 (R G), PFIS Contract FI23/00 281 (S H V), Miguel Servet Contract CP21/00 116 (R G) and co-funded by the European Union.

ORCID iDs

Gonzalo Rosa-Olmeda 0000-0002-3236-1236
Sara Hiller-Vallina 0000-0001-5973-9991
Manuel Villa 0000-0001-7000-6289
Massimo Salvi 0000-0001-7225-7401
Ricardo Gargini 0000-0003-4032-0095
Miguel Chavarrías 0000-0003-0280-3440

References

[1] Weller M, Wen P Y, Chang S M, Dirven L, Lim M, Monje M and Reifenberger G 2024 Glioma *Nat. Rev. Dis. Primers* **10** 33
[2] Becker A P, Sells B E, Haque S J and Chakravarti A 2021 Tumor heterogeneity in glioblastomas: from light microscopy to molecular pathology *Cancers* **13** 761
[3] Louis D N *et al* 2021 The 2021 who classification of tumors of the central nervous system: a summary *Neuro-Oncol.* **23** 1231–51
[4] Grochans S, Cybulska A M, Simińska D, Korbecki J, Kojder K, Chlubek D and Baranowska-Bosiacka I 2022 Epidemiology of glioblastoma multiforme–literature review *Cancers* **14** 2412
[5] Weller M *et al* 2021 Eano guidelines on the diagnosis and treatment of diffuse gliomas of adulthood *Nat. Rev. Clin. Oncol.* **18** 170–86
[6] Stupp R *et al* 2005 Radiotherapy plus concomitant and adjuvant temozolomide for glioblastoma *New Engl. J. Med.* **352** 987–96
[7] He W *et al* 2022 A review: the detection of cancer cells in histopathology based on machine vision *Comput. Biol. Med.* **146** 105636
[8] de Haan K *et al* 2021 Deep learning-based transformation of H&E stained tissues into special stains *Nat. Commun.* **12** 4884
[9] Baba A I and Câtoi C 2007 *Comparative Oncology* (The Publishing House of the Romanian Academy)
[10] Fischer E G 2020 Nuclear morphology and the biology of cancer cells *Acta Cytol.* **64** 511–9
[11] Guck J *et al* 2005 Optical deformability as an inherent cell marker for testing malignant transformation and metastatic competence *Biophys. J.* **88** 3689–98
[12] Ong M S, Deng S, Halim C E, Cai W, Tan T Z, Huang R Y-J, Sethi G, Hooi S C, Kumar A P and Yap C T 2020 Cytoskeletal proteins in cancer and intracellular stress: a therapeutic perspective *Cancers* **12** 238
[13] Ayanlaja A A, Hong X, Cheng B, Zhou H, Kanwore K, Alphayo-Kambey P, Zhang L, Tang C, Adeyanju M M and Gao D 2022 Susceptibility of cytoskeletal-associated proteins for tumor progression *Cell. Mol. Life Sci.* **79** 13
[14] Mousavikhamene Z, Sykora D J, Mrksich M and Bagheri N 2021 Morphological features of single cells enable accurate automated classification of cancer from non-cancer cell lines *Sci. Rep.* **11** 24375
[15] Izdebska M, Zielińska W, Grzanka D and Gagat M 2018 The role of actin dynamics and actin-binding proteins expression in epithelial-to-mesenchymal transition and its association with cancer progression and evaluation of possible therapeutic targets *BioMed Res. Int.* **2018** 4578373
[16] Nafe R, Franz K, Schlote W and Schneider B 2005 Morphology of tumor cell nuclei is significantly related with survival time of patients with glioblastomas *Clin. Cancer Res.* **11** 2141–8
[17] Kirishima M *et al* 2024 Prognosis prediction via histological evaluation of cellular heterogeneity in glioblastoma *Sci. Rep.* **14** 24955
[18] Neto O L A and Aldape K 2021 Morphologic and molecular aspects of glioblastomas *Neurosurgery Clin.* **32** 149–58
[19] Hijazi A, Bifulco C, Baldin P and Galon Jôme 2024 Digital pathology for better clinical practice *Cancers* **16** 1686
[20] Nahhas O S M E *et al* 2025 From whole-slide image to biomarker prediction: end-to-end weakly supervised deep learning in computational pathology *Nat. Protocols* **20** 293–316
[21] Roetzer-Pejrimovsky T, Nenning K-H, Kiesel B, Klughammer J, Rajchl M, Baumann B, Langs G and Woehrer A 2024 Deep learning links localized digital pathology phenotypes with transcriptional subtype and patient outcome in glioblastoma *GigaScience* **13** giae057
[22] Yuan Y *et al* 2024 Multimodal data integration using deep learning predicts overall survival of patients with glioma *View* **5** 20240001
[23] Unger M and Kather J N 2024 A systematic analysis of deep learning in genomics and histopathology for precision oncology *BMC Med. Genom.* **17** 48
[24] Aeffner F *et al* 2019 Introduction to digital image analysis in whole-slide imaging: a white paper from the digital pathology association *J. Pathol. Inform.* **10** 9

[25] Jiang S, Zanazzi G J and Hassanpour S 2021 Predicting prognosis and idh mutation status for patients with lower-grade gliomas using whole slide images *Sci. Rep.* **11** 16849
[26] He P, Qu A, Xiao S and Ding M 2024 Detisseg: a dual-encoder network for tissue semantic segmentation of histopathology image *Biomed. Signal Process. Control* **87** 105544
[27] Peng B *et al* 2024 Practical guidelines for cell segmentation models under optical aberrations in microscopy *Comput. Struct. Biotechnol. J.* **26** 23–39
[28] Liu Z, Mao H, Wu C-Y, Feichtenhofer C, Darrell T and Xie S 2022 A convnet for the 2020s
[29] National Cancer Institute Tinción con Hematoxilina y Eosina (available at: https://www.cancer.gov/espanol/publicaciones/diccionarios/diccionario-cancer/def/tincion-con-hematoxilina-y-eosina)
[30] Rosa-Olmeda G, Villa M, Hiller-Vallina S, Chavarrías M, Pescador F and Gargini R 2024 A microscope setup and methodology for capturing hyperspectral and RGB histopathological imaging databases *Sensors* **24** 5654
[31] Ronneberger O, Fischer P and Brox T 2015 U-Net: convolutional networks for biomedical image segmentation (arXiv:1505.04597)
[32] Chen L-C, Papandreou G, Schroff F and Adam H 2017 Rethinking atrous convolution for semantic image segmentation (arXiv:1706.05587)
[33] Chen L-C, Zhu Y, Papandreou G, Schroff F and Adam H 2018 Encoder-decoder with atrous separable convolution for semantic image segmentation (arXiv:1802.02611)
[34] Dosovitskiy A *et al* 2021 An image is worth 16 × 16 words: transformers for image recognition at scale (arXiv:2010.11929)
[35] Ridnik T, Ben-Baruch E, Noy A and Zelnik-Manor L 2021 Imagenet-21 k pretraining for the masses (arXiv:2104.10972)
[36] MMSegmentation Contributors 2020 MMSegmentation: openmmlab semantic segmentation toolbox and benchmark (available at: https://github.com/open-mmlab/mmsegmentation)
[37] Bankhead P *et al* 2017 Qupath: open source software for digital pathology image analysis *Sci. Rep.* **7** 1–7
[38] Salvi M, Michielli N, Meiburger K M, Cattelino C, Cotrufo B, Giacosa M, Giovanzana C and Molinari F 2024 cyto-Knet: an instance segmentation approach for multiple myeloma plasma cells using conditional kernels *Int. J. Imaging Syst. Technol.* **34** e22984
[39] Zhang Z and Sabuncu M 2018 Generalized cross entropy loss for training deep neural networks with noisy labels *Advances in Neural Information Processing Systems* p 31
[40] OpenCV 2025 Open cv library (available at: https://docs.opencv.org/4.x/d6/d00/tutorial_py_root.html,n.d.) (Accessed 27 March 2025)
[41] Moretti B, Alvarez S N and Grecco H E 2023 Nfinder: automatic inference of cell neighborhood in 2D and 3D using nuclear markers *BMC Bioinform.* **24** 230
[42] Breiman L 2001 Random forests *Mach. Learn.* **45** 5–32
[43] Hanahan D and Weinberg R A 2000 The hallmarks of cancer *Cell* **100** 57–70
[44] Hanahan D and Coussens L M 2012 Accessories to the crime: functions of cells recruited to the tumor microenvironment *Cancer Cell* **21** 309–22
[45] Nelson C M and Bissell M J 2006 Of extracellular matrix, scaffolds and signaling: tissue architecture regulates development, homeostasis and cancer *Annu. Rev. Cell Dev. Biol.* **22** 287–309
[46] Jamous S, Comba A, Lowenstein P R, Motsch S and Maini P K 2020 Self-organization in brain tumors: how cell morphology and cell density influence glioma pattern formation *PLoS Comput. Biol.* **16** e1007611
[47] Kirkman M A, Hunn B H M, Thomas M S C and Tolmie A K 2022 Influences on cognitive outcomes in adult patients with gliomas: a systematic review *Front. Oncol.* **12** 943600
[48] Boelders S M, Gehring K, Postma E O, Rutten G-J M and Ong L-L S 2024 Cognitive functioning in untreated glioma patients: the limited predictive value of clinical variables *Neuro-Oncol.* **26** 670–83
[49] Acs B, Rantalainen M and Hartman J 2020 Artificial intelligence as the next step towards precision pathology *J. Internal Med.* **288** 62–81
[50] Shafi S and Parwani A V 2023 Artificial intelligence in diagnostic pathology *Diagn. Pathol.* **18** 109
[51] Wang X *et al* 2024 A pathology foundation model for cancer diagnosis and prognosis prediction *Nature* **634** 970–8
[52] Zhu M 2024 Artificial intelligence in pathologic diagnosis, prognosis and prediction of prostate cancer *Am. J. Clin. Exp. Urol.* **12** 200
[53] Qaiser T, Lee C-Y, Vandenberghe M, Yeh J, Gavrielides M A, Hipp J, Scott M and Reischl J 2022 Usability of deep learning and H&E images predict disease outcome-emerging tool to optimize clinical trials *npj Prec. Oncol.* **6** 37
[54] Shi L *et al* 2023 Contribution of whole slide imaging-based deep learning in the assessment of intraoperative and postoperative sections in neuropathology *Brain Pathol.* **33** e13160
[55] Cheung E Y W, Wu R W K, Li A S M and Chu E S M 2023 AI deployment on GBM diagnosis: a novel approach to analyze histopathological images using image feature-based analysis *Cancers* **15** 5063
[56] Hou L, Gupta R, Van Arnam J S, Zhang Y, Sivalenka K, Samaras D, Kurc T M and Saltz J H 2020 Dataset of segmented nuclei in hematoxylin and eosin stained histopathology images of ten cancer types *Sci. Data* **7** 185
[57] Gerdes M J, Sevinsky C J, Sood A, Adak S, Bello M O, Bordwell A, Can A, Corwin A, Dinn S, Filkins R J 2013 Highly multiplexed single-cell analysis of formalin-fixed, paraffin-embedded cancer tissue *Proc. Natl Acad. Sci.* **110** 11982–7
[58] Yuan Y *et al* 2012 Quantitative image analysis of cellular heterogeneity in breast tumors complements genomic profiling *Sci. Trans. Med.* **4** 157ra143
[59] Johansson P *et al* 2020 A patient-derived cell atlas informs precision targeting of glioblastoma *Cell Rep.* **32** 107897
[60] Lu P, Weaver V M and Werb Z 2012 The extracellular matrix: a dynamic niche in cancer progression *J. Cell Biol.* **196** 395–406